PAPER

Spinel/perovskite cobaltite nanocomposites synthesized by combinatorial pulsed laser deposition†

Yan Chen,‡[ab] Shuchi Ojha,[c] Nikolai Tsvetkov,§[a] Dong Hun Kim,¶[c] Bilge Yildiz*[abc] and C. A. Ross*[c]

Perovskite/spinel nanocomposites have attracted great attention due to the novel properties that originate from the coupling between two oxides through their interfaces. Combinatorial pulsed laser deposition was used in this work to grow $La_{0.8}Sr_{0.2}CoO_3$ (LSC)/$CoFe_2O_4$ (CFO) nanocomposites on (001) $SrTiO_3$ (STO) under various growth conditions. At a substrate temperature of 680 °C, the LSC/CFO consisted of columns of CFO and a third phase, likely to be CoO_x, within a highly textured LSC matrix. Lowering the temperature to 600 °C resulted in highly textured LSC/CFO nanocomposites consisting of grains of LSC and CFO a few nanometers in diameter. The grain size increased with decreasing growth rate. In the nanocomposites, redistribution of Fe into the perovskite phase is expected. The strain in the CFO was impacted by the lattice match at the interfaces with the LSC, and changes in composition as well as the strain led to lower magnetic anisotropy compared with CFO films on STO. This approach can also be used to produce other novel nanocrystalline spinel/perovskite systems.

1. Introduction

Oxide heterostructures have attracted great attention because of the emergent properties that originate from the interfacial coupling between two oxides, including magnetism,[1–3] electronic properties,[4] transport,[5] and catalytic activity.[6–10] Although there has been extensive work on multilayer structures in which the interfaces are parallel to the substrate, it is also possible to co-deposit two immiscible oxides which then form a two-phase structure with specific interface orientations. These two-phase structures include self-assembled vertical nanocomposites with pillars of one phase in a matrix of the other, both of which are epitaxial with the substrate (known as a 1–3 nanocomposite),[11,12] nanosheets within a matrix (a 2–3 nanocomposite) or nanoparticles within a matrix (a 0–3 nanocomposite).[12–14] Among these oxide heterostructures, perovskite/spinel (ABO_3/CD_2O_4) nanocomposites, especially $BiFeO_3$ (BFO)/$CoFe_2O_4$ (CFO),[15–18] form well-defined vertical 1–3 structures when grown on a perovskite substrate, and in the case of BFO/CFO exhibit useful multiferroic phenomena including magnetoelectric coupling[1] and electric field-induced magnetization switching.[2]

The properties of the perovskite/spinel nanocomposite depend on the composition, geometry, strain state and crystal orientation,[12] and can be tuned widely by selection of the composition of the phases and the growth conditions. Perovskites can include a variety of substituents on the A and B sites, giving an extensive range of electronic or transport properties, but few of these compositions have been investigated as part of a nanocomposite.[6,19] Much of the reported work on perovskite/spinel nanocomposites has been based on perovskites of composition $BiFeO_3$,[15–18,20] $BaTiO_3$,[1,21] $PbTiO_3$ (ref. 22) or $(La,Sr)MnO_3$.[6,20,23–25] However, the family of cobaltite perovskites also has interesting properties such as ferromagnetism,[26] giant magnetoresistance,[27] catalytic activity[28,29] and fast oxide ion and electron transport.[30] Here $La_{0.8}Sr_{0.2}CoO_3$ (LSC) was chosen as an example of a cobaltite perovskite phase because its properties such as catalytic activity[31,32] and magnetic properties[33] are reported to be sensitive to the strain states of films. Hoffman used sputtering to deposit LSC/CFO nanocomposites, showing the potential to control the structure and composition of LSC/CFO through tuning the growth conditions.[19]

[a] *Laboratory of Electrochemical Interfaces, Cambridge, MA02139, USA*
[b] *Department of Nuclear Science and Engineering, Cambridge, MA02139, USA*
[c] *Department of Materials Science and Engineering, Massachusetts Institute of Technology, Cambridge, MA02139, USA. E-mail: byildiz@mit.edu, caross@mit.edu*
† Electronic supplementary information (ESI) available. See DOI: 10.1039/c6ce01445c
‡ New Energy Research Institute, School of Environment and Energy, South China University of Technology, Guangzhou Higher Education Mega Center, Guangzhou, Guangdong, China.
§ Graduate School of Energy, Environment, Water, and Sustainability, Korea Advanced Institute of Science and Technology, Daejeon 305-701, Korea.
¶ Department of Materials Science and Engineering, Myongji University, Korea.

Perovskite/spinel nanocomposites are often deposited by pulsed laser ablation of a composite target containing a stoichiometric mixture of the two phases.[1,2,12] This requires synthesis of a separate target for each composition. Hence, combinatorial pulsed laser deposition (cPLD) has instead been used in which two separate targets are ablated alternately to produce a sub-monolayer growth of each material. Previously we have used cPLD to grow BFO/CFO and other nanocomposites with the flexibility to tune the ratio of the two phases, the structure, strain state and resulting properties.[17,18,34–36] In this work, LSC/CFO nanocomposites were grown on $SrTiO_3$ (STO) (001) substrates using cPLD under a range of deposition conditions, and the structure of the nanocomposite was characterized. High temperature growth produced columnar intrusions of CFO and CoO_x within a highly textured LSC matrix. Decreasing the growth temperature instead formed intermixed LSC and CFO grains with size of a few nanometers, both highly textured with (00l) out-of-plane orientation. The magnetic properties of the LSC/CFO nanocomposite were characterized and were correlated with the strain state of the CFO. Additionally, $Ba_{0.5}Sr_{0.5}Co_{0.8}Fe_{0.2}O_3$ (BSCF)/CFO nanocomposites were synthesized under similar growth conditions (see ESI†), demonstrating the capability of producing other nanocrystalline spinel/cobalt-perovskite systems.

2. Experimental methods

The spinel/perovskite nanocomposites were deposited by combinatorial PLD, as shown in Fig. 1. To obtain samples with different spinel/perovskite ratio from one deposition, one material (perovskite phase) was deposited with n_1 pulses and the other material (spinel) was deposited with n_2 pulses (Fig. 1(a)). This sequence was repeated N times until the desired thickness is obtained. The thickness of each layer that was deposited in each sequence was below one unit cell. Between each set of pulses, the targets and substrate holder were moved such that a composition gradient was formed across a distance of about 5 cm. A set of samples was produced during each deposition run with the perovskite to spinel ratio for each sample depending on n_1/n_2 and the position of the substrate on the holder. To obtain several samples with the same composition, the substrate holder was rotated during deposition (Fig. 1(b)). A KrF excimer laser source (λ = 248 nm) was employed with repetition rate range from 2–10 Hz. The base pressure in the chamber was below 5×10^{-6} Torr and the working pressure was 10 mTorr of oxygen. After growth, the films were cooled down to room temperature in 2 Torr oxygen pressure. Several growth temperatures were tested ranging from 560 °C to 680 °C. The substrates used in this work were STO (001) single crystal substrates.

The surfaces and cross sectional structures of the nanocomposites were characterized with scanning electron microscopy (SEM). A Helios Nanolab 600 Dual Beam Focused Ion Beam Milling System (FIB) was used to prepare cross sections with a Ga^+ ion beam, after a Pt layer had been deposited onto the surface for protection. The crystal structure of the samples was determined using a Rigaku Smartlab Multipurpose Diffractometer, equipped with a 9 kW rotating anode X-ray source and incident-beam Ge (022) double-bounce monochromator. The reciprocal space map (RSM) was measured using a Bruker D8 Discover diffractometer, with a Göbel mirror, four-bounce Ge (022) channel-cut monochromator, Eulerian cradle, and a scintillation counter, using Cu Kα_1 radiation.

Samples for transmission electron microscopy (TEM) measurements were fabricated in the Helios Nanolab 600 dual beam focused ion beam milling system. The Ga^+ focused ion beam was operated at a voltage and current in the range of 30–2 keV and 9.5 nA–28 pA, respectively. The FIB cuts were made parallel to the substrate edge in the <001> directions. TEM measurements were performed using a JEOL 2010 FEG microscope. The magnetic properties of the films were measured using vibrating sample magnetometry (VSM, ADE model 1660) at room temperature.
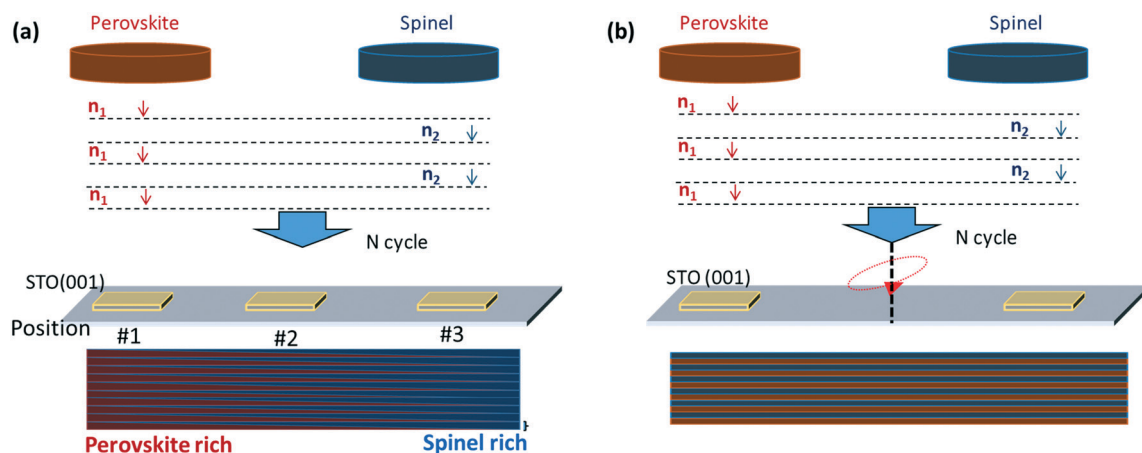

Fig. 1 Schematics showing the growth process of spinel and perovskite composite by combinatorial pulsed laser deposition; (a) samples with different perovskite to spinel ratio grown during the same deposition; (b) by rotating the substrates, several samples are grown with the same perovskite to spinel ratio.

3. Results and discussion

3.1 LSC/CFO nanocomposite grown by combinatorial PLD at 680 °C

LSC/CFO nanocomposites with different LSC to CFO ratios were grown by cPLD at 680 °C substrate temperature with n_1 and n_2 both 50 pulses in each deposition cycle and $N = 200$ cycles (Fig. 1(a)). Fig. 2(a)–(c) shows SEM images of the LSC/CFO surface, with the CFO ratio increasing from sample #1 to sample #3. Square inclusions with different sizes were embedded in a dense thin film matrix, as shown in Fig. 2(g) for sample #1. Dilute hydrochloric acid (HCl) was used to etch the films. Fig. 2(d)–(f) presents SEM images of the LSC/CFO nanocomposites after etching. The matrix material was preferentially etched away. While the small inclusions are almost unchanged after etching, there are small holes visible in the center of the larger inclusions, seen in Fig. 2(d). HRXRD results (Fig. S1†) showed that the LSC phase in our LSC/CFO composite film was highly textured with (001) orientation. The peaks from CFO cannot be seen in the HRXRD data measured with monochromatic X-rays. Using XRD without the monochromator optics, a small (004) peak from the CFO phase can be observed (Fig. 2(h)). After HCl etching, the LSC (002) peaks disappear while the CFO (004) peaks remain, as shown for sample #2 (Fig. 2(h)).

The effect of etching on the peaks visible in the HRXRD scan identifies the matrix to be a highly textured LSC phase, whereas the smaller square inclusions and the shells of the larger inclusions were likely CFO spinel. There is a third phase at the center of the large inclusions which can be removed by HCl etching. Due to the small volume fraction, the phase cannot be identified from XRD. However, the structure resembles the sputtered LSC/CFO composite structure grown by Hoffmann et al.,[19] in which CoO_x was present. CoO_x can be removed readily by an HCl etch. Therefore, we conclude the LSC/CFO nanocomposite grown at 680 °C exhibited phase separation of CFO and LSC but additional CoO_x was formed at the cores of the CFO pillars. In comparison, $Cu/SrO/Sr(Ti,Cu)O_3$ is another example of a core–shell-matrix 3-phase epitaxial nanocomposite.[35]

3.2 LSC/CFO nanocomposite grown by combinatorial PLD at 600 °C

3.2.1 Crystal structure.
The deposition temperature was reduced to 600 °C in order to minimize the growth of the unwanted phases, yielding an composite structure with qualitative structural differences compared to the nanocomposite grown at 680 °C (growth at 560 °C produced similar structures to those grown at 600 °C, without the pillars seen at 680 °C). Films were grown with substrate rotation to give a uniform composition (Fig. 1(b)). The growth rates predict a volume fraction of 46% for the CFO. Fig. 3(a) and (b) give SEM images of the surface and cross sectional structure of the 600 °C nanocomposites, which showed no obvious columnar phase separation. HRXRD (Fig. 3(f)), however, shows peaks corresponding to both CFO phase and LSC phase, both highly textured with (00l) orientation on the STO (001) substrate. High-resolution TEM (HRTEM) cross-sectional images of the LSC/CFO film are shown in Fig. 3(c). Two types of atomic arrangements which can be attributed to perovskite and spinel structures are shown in the inset of Fig. 3(c). TEM diffraction (Fig. S2†) suggests the nanocrystals of the two phases are highly textured on the substrate, despite lattice defects. The dark areas observed in the TEM images are believed to be a result of the inhomogeneous strain in the film, but may also be related to artifacts of ion milling.

Both HRXRD and HRTEM results therefore indicate the successful synthesis of a two-phase LSC/CFO nanocomposite,
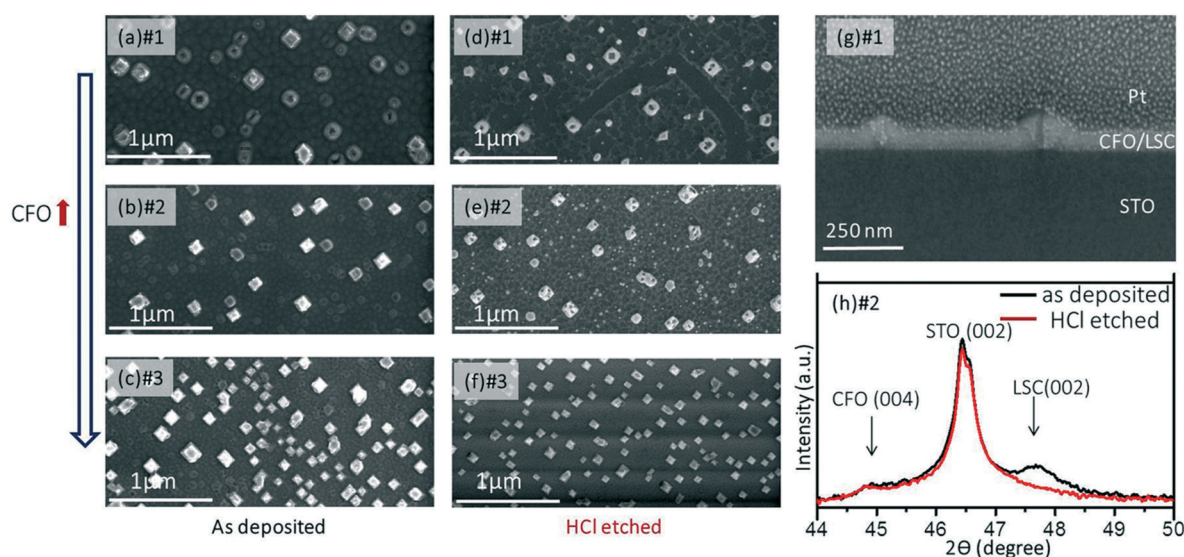

Fig. 2 (a–c) Top surface SEM image of LSC/CFO grown at 680 °C, with the fraction of CFO increasing from sample #1 to sample #3; (d–f) top surface SEM image of LSC/CFO samples #1 to #3 after HCl etching; (g) cross-sectional SEM image of LSC/CFO sample #1, in which the two large features in the film surface represent CFO surrounding CoO_x; (h) 2θ–ω scan of LSC/CFO sample #2 as deposited and after HCl etching.
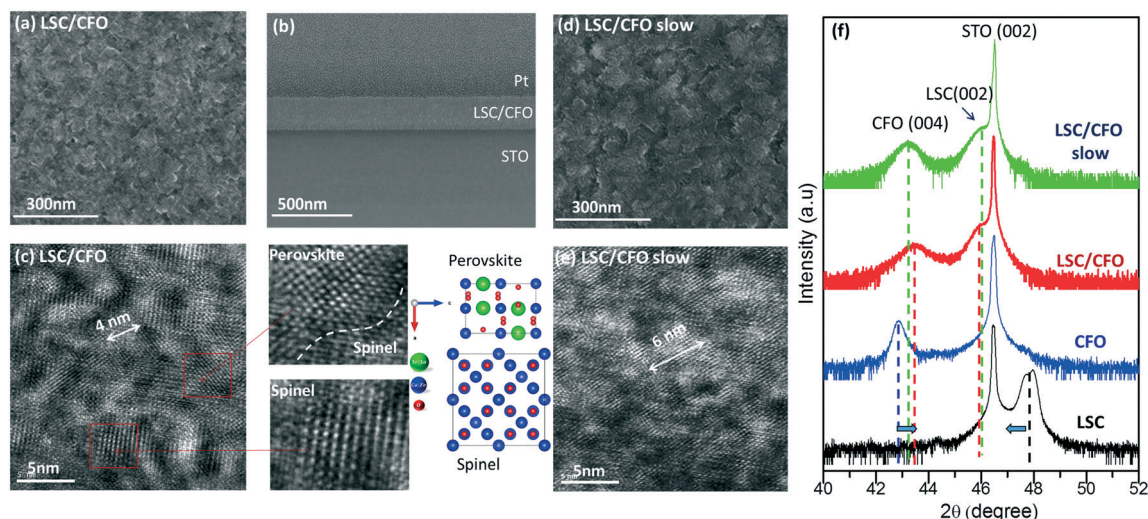
Fig. 3 (a) Top surface and (b) cross sectional SEM image of LSC/CFO nanocomposite grown at 600 °C, using 10 Hz laser frequency ($n_1 = 50$; $n_2 = 200$, $N = 300$); (c) HRTEM image of LSCF/CFO, in which the insets show the structure of the LSC and CFO grains; (d) top surface SEM image and (e) HRTEM image of LSC/CFO grown with 2 Hz laser frequency ($n_1 = 50$; $n_2 = 200$, $N = 300$); (f) comparison of the 2θ–ω scan of LSC/CFO with different growth rates, 10 Hz and 2 Hz (slow), and of CFO single phase and LSC single phase films grown at 600 °C, 10 Hz.

but without the columnar growth seen at 680 °C. Instead, the films consisted of grains of the individual phases about 4 nm in diameter (Fig. 3(c)), corresponding to a 0–0 nanocomposite. This change in morphology may be a result of the slower diffusion kinetics during deposition. If surface diffusion is inhibited, adatoms cannot reach pre-existing columnar grains and new grains nucleate instead giving a film consisting of intermixed nanocrystals. To further explore the growth mechanism, we decreased the growth rate by a factor of 5 by decreasing the laser repetition rate from 10 Hz to 2 Hz. The surface SEM image and HRTEM image of the LSC/CFO films fabricated with slower growth rates is showed in Fig. 3(d and e). The films grown at a slower rate showed larger grains about 6 nm in diameter, but still did not form a vertical nanocomposite.

3.2.2 Strain in LSC/CFO nanocomposite. Table 1 summarizes the lattice parameters of LSC and CFO single phase and nanocomposite films. Films of single phase CFO and LSC grown under the same conditions of pulse rate, pulse energy and temperature as the nanocomposite (600 °C, 10 Hz) were highly textured on STO (001) substrate. The out-of-plane lattice parameter of the CFO film was 0.8431 nm, which exceeds that of bulk CFO ($a_{CFO} = 0.8391$ nm). From the reciprocal

space map of CFO on STO (Fig. 4), the CFO in-plane lattice parameter was 0.8369 nm, indicating that the CFO film is not fully strained to match the in-plane lattice parameter of the STO substrate ($a_{STO} = 0.3905$ nm). The CFO is therefore under in-plane compression and has a tetragonal distortion ($c/a = 1.007$).

In contrast, the out of plane lattice parameter of an LSC thin film ($2a_{LSC} = 0.7597$ nm) grown on STO at 600 °C is smaller than that of bulk LSC (bulk LSC: $2a_{LSC} = 0.7680$ nm measured from the target),[6] which is likely due to the tensile in-plane lattice strain imposed by the STO substrate.

In the LSC/CFO nanocomposites made at 600 °C the out-of-plane lattice parameter of CFO was smaller than that of the single phase film and bulk CFO. The CFO peaks in the reciprocal space mapping of the nanocomposite were weak (Fig. S3†), precluding measurement of the in-plane lattice parameter, but the in-plane and out-of-plane lattice parameters of the LSC/CFO nanocomposite were estimated based on the HRTEM image (Table 1). This measurement suggests an out-of-plane tensile deformation in the CFO.

The out-of-plane lattice parameter of LSC was considerably larger than bulk, and the LSC (002) peak shifted from the right of the STO (002) peak to the left in the 2θ–ω scan (Fig. 3(f)). The Young's modulus of LSC and CFO are quite

Table 1 In-plane (IP) and out-of-plane (OP) lattice parameters of bulk CFO and LSC, single phase films on STO, and nanocomposites on STO determined from HRXRD and HRTEM

| Sample	OP lattice parameter of CFO, nm	IP lattice parameter of CFO, nm	c/a	OP lattice parameter of STO, LSC, nm	IP lattice parameter of STO, LSC, nm
Bulk STO ($2a_{STO}$)				0.7810	
Bulk LSC ($2a_{LSC}$)				0.7680	
LSC thin film ($2a_{LSC}$)				0.7597	
Bulk CFO	0.8391	0.8391	1.00		
CFO thin film	0.8431	0.8369	1.007		
LSC/CFO 10 Hz	0.8318 (XRD), 0.84 (TEM)	0.81 (TEM)	1.04 (TEM)	LSC: 0.7892 (XRD), 0.79 (TEM)	LSC: 0.79 (TEM)
LSC/CFO 2 Hz	0.8370 (XRD), 0.84 (TEM)	0.82 (TEM)	1.02 (TEM)	LSC: 0.7890 (XRD), 0.79 (TEM)	LSC: 0.79 (TEM)
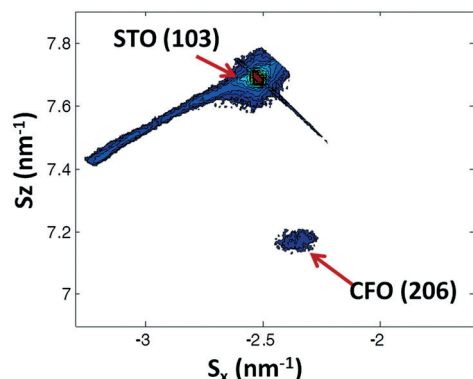
Fig. 4 X-ray diffraction reciprocal space map of CFO single phase on STO (100) at 600 °C, using 10 Hz laser frequency.

similar, with ~140 GPa for LSC[37] and ~141.6 Gpa for CFO.[38] Epitaxy of LSC with CFO in the out-of-plane direction would lead to compressive strain in CFO and tensile in LSC. However the measured distortion is large compared to the bulk lattice parameter. Furthermore, TEM measurement of lattice parameters showed no clear tetragonal distortion of the LSC, and its unit cell volume exceeded that of bulk or single phase thin film LSC. In our previous work,[36] we observed elemental redistribution in $BiFeO_3$–MgO and $BiFeO_3$–$MgAl_2O_4$ nanocomposite films grown by combinatorial PLD such that the pillars consisted of $Mg(Al,Fe)_2O_4$. Hoffman[19] also saw in LSC/CFO grown by sputtering that Fe enters the perovskite. Therefore, it is possible that besides different strain states, the LSC in our LSC/CFO nanocomposite has a different composition or oxygen content compared to single phase films, *e.g.* from the incorporation of Fe into the LSC to become $La_{0.8}Sr_{0.2}Co_{1-x}Fe_xO_3$ (LSCF). The lattice parameter of LSCF was reported to increase with Fe content,[39] which is consistent with our speculation of Fe incorporation into LSC leading to a larger lattice parameter than bulk LSC. This would also lead to Co-rich CFO in the nanocomposite. At higher growth temperature, the amount of Fe that diffuses from CFO into LSC increases, which is likely to be the reason for the formation of CoO_x at 680 °C (section 3.1).

When the deposition rate of the nanocomposite was reduced by using 2 Hz laser repetition rate, the CFO out-of-plane lattice parameter was intermediate between that of single phase CFO on STO and that of the nanocomposite grown at 10 Hz. This is attributed to strain relaxation during the slower growth. The LSC lattice parameter in the LSC/CFO showed little change between the two samples.

3.2.3 Magnetic properties of LSC/CFO nanocomposites. Fig. 5 shows the magnetic hysteresis loops for single phase CFO on STO as well as LSC/CFO nanocomposites on STO made at 600 °C at two different growth rates. The single phase CFO has a magnetization of 150 emu cm^{-3} at 12 kOe field. This value is lower than expected for the saturation magnetization M_s of bulk CFO of 400 emu cm^{-3},[40] but the CFO film is not saturated at this field and the data represent a minor hysteresis loop with magnetization below M_s. Using wavelength dispersive spectrometry, the stoichiometry (Co : Fe

ratio) of the CFO films was quantified to be around 0.74, which is larger than the ideal $CoFe_2O_4$ stoichiometry (0.5). Such deviations in the stoichiometry, as well as cation disorder between the tetrahedral and octahedral sites, can lower M_s and affect other magnetic properties.[41]

The magnetic anisotropy of the CFO includes contributions from shape, magnetocrystalline anisotropy and magnetoelastic anisotropy. For the (001)-oriented film the magnetocrystalline anisotropy energy is equivalent for in-plane and out-of-plane directions. The shape anisotropy field $H_{sh} = 4\pi M_s$ (cgs units) yields a maximum value for $H_{sh} = 5$ kOe based on $M_s = 150$ emu cm^{-3}. The magnetoelastic anisotropy field is given by $H_{me} = \dfrac{3Y\varepsilon_{100}\lambda_{100}}{M_s}$ where λ_{100} is the magnetostriction coefficient, Y is the Young's modulus and ε_{100} is the in-plane strain assuming a volume-conserving strain. $Y_{CFO} = 141.6$ GPa, $\lambda_{001,CFO} = (-250$ to $-590) \times 10^{-6}$ (ref. 42) and $\varepsilon_{100} = 0.005$ for a tetragonally distorted unit cell with $c/a = 1.007$, yielding $H_{me} = \sim 1–2.5$ kOe for the single crystal film. Both the magnetoelastic anisotropy and the shape anisotropy favor an in-plane easy axis, while the magnetocrystalline anisotropy favors magnetization along <111> since K_1, the first order term in the magnetocrystalline anisotropy is negative. Both loops show hysteresis with a low-field step that may indicate part of the film is easier to magnetize, for example due to partial strain relaxation as indicated in the RSM.

The nanocomposites made at 600 °C show much lower saturation fields than the single phase film, and an in-plane easy axis. The lower anisotropy is consistent with the more equiaxed grain shape and the lower strain compared with the single-crystal film. The small grain size may also facilitate thermally assisted reversal. The LSC/CFO nanocomposites saturate at around 30–60 emu cm^{-3}, when normalized to the volume of the entire film. This gives a saturation magnetization for CFO of around 60–120 emu cm^{-3} based on a 46% volume fraction, lower than for the CFO film. This may be an indication of a Fe depletion of CFO stoichiometry in the nanocomposite, as reported by Hoffman.[19] An LSC single phase film had negligible M_s below ~2 emu cm^{-3}, as shown in Fig. S6.†

For comparison, the loops of the LSC/CFO nanocomposites grown at 680 °C are given in Fig. S5.† The loops are isotropic without hysteresis, with a significantly lower saturation magnetization than that of the nanocomposites grown at 600 °C. The magnetization increased with CFO content as expected. Etching lowered the magnetization by a factor of 2.3–2.8. Since etching removes the perovskite phase but not the spinel, we conclude that some of the magnetic signal originated in the perovskite phase, presumably as a result of the cation interdiffusion between the phases since single-phase LSC has little magnetic moment.

3.3 Discussion

BFO/CFO nanocomposites grown by cPLD are well known to exhibit columnar growth at a temperature as low as 560 °C,
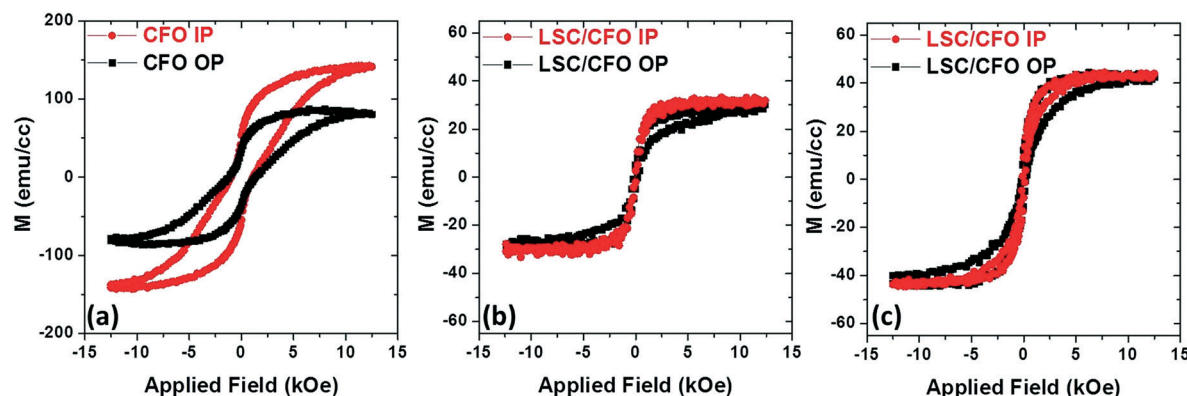
Fig. 5 In-plane (IP) and out-of-plane (OP) hysteresis loops of (a) CFO, (b and c) LSC/CFO grown at 600 °C, using (b) 10 Hz and (c) 2 Hz laser repetition rate. M is normalized to the total volume of the film.

making a structure of CFO pillars in BFO matrix.[18] In this work, even at 600 °C the LSC/CFO nanocomposites formed a mixture of small grains, highly textured with (001) orientation on the substrate. The reason for such a difference is likely due to a smaller diffusion distance of LSC compared with BFO at this temperature. Zheng *et al.*[43] modeled the growth of BFO/CFO nanocomposites as a diffusion process, assuming the transport is limited to the solid–vapor interface and diffusion within the bulk is negligible. Based on the BFO and CFO nanopillar sizes as a function of growth temperature, they identify the activation energy of adatom diffusion of CFO and BFO to be 1.66 eV and 0.58 eV, respectively, which were believed to be related to the diffusion barrier to form a pillar structure. Based on these activation energies, Comes *et al.*[44] further estimated the adatom diffusion length of CFO at 600 °C to be around 55 nm. In our case, the domain size of each phase in LSC/CFO nanocomposite is a few nm, suggesting the diffusion length of LSC at 600 °C is much smaller than that of CFO. Such differences may be related to the higher diffusion coefficients of Fe and Co than those of Sr and La, as quantified for LSC by Kubicek *et al.*[45] The increase of grain size for slower growth rate is also an indication that the growth of the nanocomposite is limited by diffusion. When the temperature is higher (680 °C), the diffusion might become fast enough to enable the formation of nanopillars as we observed in section 3.1. However, the higher temperature also introduced the formation of a third phase in the nanocomposite.

The LSC/CFO nanocomposites consist of uniformly distributed nanoscale grains of two phases, and can be described as 0–0 nanocomposites. Due to the small grain size, each phase in the nanocomposite can sustain a large strain. These results suggest that the 0–0 nanocomposite could serve as platform for strain engineering of material properties. To demonstrate the capability of producing other nanocrystalline spinel/perovskite systems, we also synthesized nanocomposites made of CFO and $Ba_{0.5}Sr_{0.5}Co_{0.8}Fe_{0.2}O_3$ (BSCF),[46] one of the most active cobaltite cathodes with very high oxygen exchange coefficient. The same deposition procedure ($T = 600$ °C, $n_1 = 50$, $n_2 = 200$, $N = 300$, $f = 10$ Hz) as in Fig. 1(b) was used to grow

a BSCF/CFO nanocomposite structure by replacing the LSC target with a BSCF target. The BSCF and CFO were phase-separated during deposition with the grain size similar to the case of LSC/CFO (~4 nm), and were highly textured in the (00*l*) orientation (Fig. S4(b–d)†). The out-of-plane lattice parameter of CFO in the BSCF/CFO nanocomposite (0.8388 nm) is larger than that of CFO in LSC/CFO (0.8318 nm), which is consistent with the larger lattice parameter of BSCF (bulk BSCF: $2a_{BSCF} = 0.792$ nm)[47] than that of LSC (bulk LSC: $2a_{LSC} = 0.7680$ nm).[6] The BSCF/CFO nanocomposite shows low coercivity and saturation field below 2 kOe, with little anisotropy. This may be attributed to the small equiaxed grains and the low strain state seen in Fig. S4(e).†

4. Conclusion

Combinatorial PLD was used to grow $La_{0.8}Sr_{0.2}CoO_3$ (LSC)/ $CoFe_2O_4$ (CFO) nanocomposites on $SrTiO_3$ (001) substrates under various growth conditions. At a substrate temperature of 680 °C the LSC/CFO consisted of columns of CFO and CoO_x within a highly textured LSC matrix, but at 600 °C, LSC/CFO nanocomposites consisted of grains of LSC and CFO a few nanometers in diameter, and both phases were highly textured. The grain size increased with decreasing growth rate. The magnetic anisotropy and magnetization of the nanocrystalline CFO was smaller than that of single phase CFO film on STO, which is likely due to the strain relaxation and Fe diffusion from CFO into LSC. $Ba_{0.5}Sr_{0.5}Co_{0.8}Fe_{0.2}$ (BSCF)/CFO nanocomposites were also synthesized using similar growth conditions, and demonstrated near-bulk CFO lattice parameter and a low magnetic anisotropy. The formation of nanocrystalline composites instead of columnar structures is attributed to limited diffusion on the surface of the growing film. This synthesis approach could be applied to produce other strained nanocrystalline spinel/perovskite systems, which may be useful as catalysts or multiferroics. Our ongoing effort is to characterize the electrochemical catalytic activity of those perovskite/spinel composites through strain engineering by choosing appropriate components in the structure.

Acknowledgements

References

1 H. Zheng, J. Wang, S. E. Lofland, Z. Ma, L. Mohaddes-Ardabili, T. Zhao, L. Salamanca-Riba, S. R. Shinde, S. B. Ogale, F. Bai, D. Viehland, Y. Jia, D. G. Schlom, M. Wuttig, A. Roytburd and R. Ramesh, *Science*, 2004, **303**, 661–663.

2 F. Zavaliche, H. Zheng, L. Mohaddes-Ardabili, S. Y. Yang, Q. Zhan, P. Shafer, E. Reilly, R. Chopdekar, Y. Jia, P. Wright, D. G. Schlom, Y. Suzuki and R. Ramesh, *Nano Lett.*, 2005, **5**, 1793–1796.

3 R. Ramesh and N. A. Spaldin, *Nat. Mater.*, 2007, **6**, 21–29.

4 Y. Chen, Z. H. Cai, Y. Kuru, W. Ma, H. L. Tuller and B. Yildiz, *Adv. Energy Mater.*, 2013, **3**, 1221–1229.

5 X. X. Guo and J. Maier, *Adv. Mater.*, 2009, **21**, 2619–2631.

6 W. Ma, J. J. Kim, N. Tsvetkov, T. Daio, Y. Kuru, Z. H. Cai, Y. Chen, K. Sasaki, H. L. Tuller and B. Yildiz, *J. Mater. Chem. A*, 2015, **3**, 207–219.

7 J. Yoon, S. Cho, J. H. Kim, J. Lee, Z. X. Bi, A. Serquis, X. H. Zhang, A. Manthiram and H. Y. Wang, *Adv. Funct. Mater.*, 2009, **19**, 3868–3873.

8 M. Sase, K. Yashiro, K. Sato, J. Mizusaki, T. Kawada, N. Sakai, K. Yamaji, T. Horita and H. Yokokawa, *Solid State Ionics*, 2008, **178**, 1843–1852.

9 E. J. Crumlin, E. Mutoro, S. J. Ahn, G. J. la O′, D. N. Leonard, A. Borisevich, M. D. Biegalski, H. M. Christen and Y. Shao-Horn, *J. Phys. Chem. Lett.*, 2010, **1**, 3149–3155.

10 X. Zou, H. Fan, Y. Tian and S. Yan, *CrystEngComm*, 2014, **16**, 1149–1156.

11 W. R. Zhang, A. P. Chen, Z. K. Bi, Q. X. Jia, J. L. MacManus-Driscoll and H. Y. Wang, *Curr. Opin. Solid State Mater. Sci.*, 2014, **18**, 6–18.

12 J. L. MacManus-Driscoll, *Adv. Funct. Mater.*, 2010, **20**, 2035–2045.

13 Y. Li, Z. Wang, J. Yao, T. Yang, Z. Wang, J. M. Hu, C. Chen, R. Sun, Z. Tian, J. Li, L. Q. Chen and D. Viehland, *Nat. Commun.*, 2015, **6**, 6680.

14 M. Liu, X. Li, J. Lou, S. Zheng, K. Du and N. X. Sun, *J. Appl. Phys.*, 2007, **102**, 083911.

15 Z. G. Wang, Y. X. Li, R. Viswan, B. L. Hu, V. G. Harris, J. F. Li and D. Viehland, *ACS Nano*, 2013, **7**, 3447–3456.

16 Z. Wang, Y. Yang, R. Viswan, J. Li and D. Viehland, *Appl. Phys. Lett.*, 2011, **99**, 043110.

17 N. M. Aimon, D. H. Kim, H. K. Choi and C. A. Ross, *Appl. Phys. Lett.*, 2012, **100**, 092901.

18 D. H. Kim, N. M. Aimon and C. A. Ross, *APL Mater.*, 2014, **2**, 081101.

19 J. Hoffmann, S. Schnittger, J. Norpoth, S. Raabe, T. Kramer and C. Jooss, *J. Mater. Res.*, 2012, **27**, 1462–1470.

20 J. L. MacManus-Driscoll, P. Zerrer, H. Y. Wang, H. Yang, J. Yoon, A. Fouchet, R. Yu, M. G. Blamire and Q. X. Jia, *Nat. Mater.*, 2008, **7**, 314–320.

21 H. M. Zheng, J. Kreisel, Y. H. Chu, R. Ramesh and L. Salamanca-Riba, *Appl. Phys. Lett.*, 2007, **90**, 113113.

22 C. Y. Tsai, H. R. Chen, F. C. Chang, W. C. Tsai, H. M. Cheng, Y. H. Chu, C. H. Lai and W. F. Hsieh, *Appl. Phys. Lett.*, 2013, **102**, 132905.

23 M. Fan, W. Zhang, F. Khatkhatay, L. G. Li and H. Wang, *J. Appl. Phys.*, 2015, **118**, 065302.

24 W. R. Zhang, A. P. Chen, F. Khatkhatay, C. F. Tsai, Q. Su, L. Jiao, X. H. Zhang and H. Y. Wang, *ACS Appl. Mater. Interfaces*, 2013, **5**, 3995–3999.

25 W. R. Zhang, A. P. Chen, J. Jian, Y. Y. Zhu, L. Chen, P. Lu, Q. X. Jia, J. L. MacManus-Driscoll, X. H. Zhang and H. Y. Wang, *Nanoscale*, 2015, **7**, 13808–13815.

26 J. W. Freeland, J. X. Ma and J. Shi, *Appl. Phys. Lett.*, 2008, **93**, 212501.

27 J. Wu, J. W. Lynn, C. J. Glinka, J. Burley, H. Zheng, J. F. Mitchell and C. Leighton, *Phys. Rev. Lett.*, 2005, **94**, 037201.

28 A. J. Jacobson, *Chem. Mater.*, 2010, **22**, 660–674.

29 A. Aguadero, L. Fawcett, S. Taub, R. Woolley, K. T. Wu, N. Xu, J. A. Kilner and S. J. Skinner, *J. Mater. Sci.*, 2012, **47**, 3925–3948.

30 J. Mizusaki, J. Tabuchi, T. Matsuura, S. Yamauchi and K. Fueki, *J. Electrochem. Soc.*, 1989, **136**, 2082–2088.

31 M. Kubicek, Z. H. Cai, W. Ma, B. Yildiz, H. Hutter and J. Fleig, *ACS Nano*, 2013, **7**, 3276–3286.

32 Z. H. Cai, Y. Kuru, J. W. Han, Y. Chen and B. Yildiz, *J. Am. Chem. Soc.*, 2011, **133**, 17696–17704.

33 D. Fuchs, E. Arac, C. Pinta, S. Schuppler, R. Schneider and H. V. von Lohneysen, *Phys. Rev. B: Condens. Matter Mater. Phys.*, 2008, **77**, 014434.

34 D. H. Kim, N. M. Aimon, X. Y. Sun and C. A. Ross, *Adv. Funct. Mater.*, 2014, **24**, 2334–2342.

35 D. H. Kim, X. Y. Sun, N. M. Aimon, J. J. Kim, M. J. Campion, H. L. Tuller, L. Kornblum, F. J. Walker, C. H. Ahn and C. A. Ross, *Adv. Funct. Mater.*, 2015, **25**, 3091–3100.

36 D. H. Kim, X. Sun, T. C. Kim, Y. J. Eun, T. Lee, S. G. Jeong and C. A. Ross, *ACS Appl. Mater. Interfaces*, 2016, **8**, 2673–2679.

37 Y. Kimura, T. Kushi, S. Hashimoto, K. Amezawa and T. Kawada, *J. Am. Ceram. Soc.*, 2012, **95**, 2608–2613.

38 V. J. Folen, *Magnetic and Other Properties of Oxides and Related Compounds*, Springer-Verlag, 1982, Landolt-Bornstein, vol. 3, part 4b.

39 S.-i. Hashimoto, Y. Fukuda, M. Kuhn, K. Sato, K. Yashiro and J. Mizusaki, *Solid State Ionics*, 2011, **186**, 37–43.

40 Y. Suzuki, R. B. van Dover, E. M. Gyorgy, J. M. Phillips, V. Korenivski, D. J. Werder, C. H. Chen, R. J. Felder, R. J. Cava, J. J. Krajewski and W. F. Peck, *J. Appl. Phys.*, 1996, **79**, 5923–5925.

41 A. K. Axelsson, M. Valant, L. Fenner, A. S. Wills and N. M. Alford, *Thin Solid Films*, 2009, **517**, 3742–3747.

42 R. M. Bozorth, E. F. Tilden and A. J. Williams, *Phys. Rev.*, 1955, **99**(6), 1788–1798.

43 H. M. Zheng, F. Straub, Q. Zhan, P. L. Yang, W. K. Hsieh, F. Zavaliche, Y. H. Chu, U. Dahmen and R. Ramesh, *Adv. Mater.*, 2006, **18**, 2747–2752.

44 R. Comes, H. X. Liu, M. Kholchov, R. Kasica, J. W. Lu and S. A. Wolf, *Nano Lett.*, 2012, **12**, 2367–2373.

45 M. Kubicek, G. M. Rupp, S. Huber, A. Penn, A. K. Opitz, J. Bernardi, M. Stoger-Pollach, H. Hutter and J. Fleig, *Phys. Chem. Chem. Phys.*, 2014, **16**, 2715–2726.

46 Z. P. Shao, S. M. Haile, J. Ahn, P. D. Ronney, Z. L. Zhan and S. A. Barnett, *Nature*, 2005, **435**, 795–798.

47 B. Wei, Z. Lu, X. Q. Huang, J. P. Miao, X. Q. Sha, X. S. Xin and W. H. Su, *J. Eur. Ceram. Soc.*, 2006, **26**, 2827–2832.